Article

Digital Analysis with the Help of an Integrated UAV System for the Surveillance of Fruit and Wine Areas

George Ipate [1] , Catalina Tudora [2] and Filip Ilie [3,*]

1 Department of Biotechnical Systems, National University of Science and Technology Polytechnic Bucharest, 060042 Bucharest, Romania; george.ipate@upb.ro
2 National Institute of Research, Development for Machines and Installations Designed for Agriculture and Food Industry, INMA Bucharest, 013811 Bucharest, Romania; tudora@inma.ro
3 Department of Machine Elements and Tribology, National University of Science and Technology Polytechnic Bucharest, 060042 Bucharest, Romania
* Correspondence: filip.ilie@upb.ro

Abstract: The main purpose of this study was to create a prototype of an unmanned aerial system equipped with intelligent hardware and software technologies necessary for surveillance and monitoring the health and growth of crops from orchards with vines and fruit trees. Using low-cost sensors that accurately measure ultraviolet solar radiation was an important objective. The device, which needed to be attached to the commercial DJI Mini 4 Pro drone, had to be small, portable, and have low energy consumption. For this purpose, the widely used Vishay VEML6075 digital optical sensor was selected and implemented in a prototype, alongside a Raspberry Pi Zero 2 W minicomputer. To collect data from these sensors, a program written in Python was used, containing specific blocks for data acquisition from each sensor, to facilitate the monitoring of ultraviolet (UV) radiation, or battery current. By analyzing the data obtained from the sensors, several important conclusions were drawn that may provide valuable pathways for the further development of mobile or modular equipment. Furthermore, the plantation state analysis results with proposed models in the geographic information system (GIS) environment are also presented. The visualization of maps indicating variations in vegetation conditions led to identifying problems such as hydric stress.

Keywords: drone; sensors; UV radiation; remote sensing; GIS; unmanned aerial system (UAS); crop; orchard; vineyards monitoring; agricultural surveillance; plant health

1. Introduction

By developing a modular system-integrated unmanned aerial vehicle (UAV) for monitoring orchards, vineyards, and environmental parameters, we aimed to produce an advanced aerial technology solution designed to facilitate the efficient management and surveillance of fruit trees and vine crops. Our prototype system uses low-cost commercial drones equipped with cutting-edge technology to collect valuable data and information about plant health and environmental conditions; it is accessible, efficient technology, and a viable alternative for ordinary farmers to the expensive and complex systems presently used. Such a modular system can be customized according to the needs of each farm, adapting to the specific conditions of crops in orchards and vineyards. By storing and analyzing collected data, it will enable farmers to make decisions and implement effective management strategies, to increase productivity, and improve the quality of the harvest.

Drones equipped with sensors and high-resolution cameras capture detailed aerial images of orchards and vineyards, covering large areas of land, including regions that are difficult to access using traditional surveillance and monitoring methods [1–3]. In [4–6], an analysis is presented of the latest technologies and innovations concerning the equipping of drones with sensors, which are essential for monitoring and data collection. Additionally,

Popescu et al. [7] analyze the implementation of the latest neural network systems in UAV-based orchard monitoring. The complex features, databases, software, and performance of such applications are highlighted. A low-cost mobile device, based on a UAV and a Geiger–Müller counter ZP 1200 for real-time detection of environmental gamma radiation, was developed by Signing et al. [8]. Ji et al. [9] proposed and developed a technical solution based on a drone for monitoring radiation in contaminated areas. Similarly, Kezoudi et al. [10] presented a comprehensive study on the development of new sensor systems implemented in UAV measurements in environmental sciences and the necessity of their integration into global networks.

UV-B radiation, which is part of the ultraviolet spectrum of sunlight, can significantly affect fruit trees and grapevines in orchards, with the effects being both negative and positive, depending on the intensity of the radiation and the susceptibility of the exposed plant species. UV-B radiation can influence the growth of fruit trees by reducing leaf area and total biomass [11]. Similar responses are observed also in grapevines, having potential impacts on photosynthetic processes, which can negatively influence fruits and grape yield and quality [12].

Effects on photosynthesis and physiology include a reduction in the photosynthetic efficiency of plants due to damage to chloroplasts and inhibition of photosynthetic affecting the water balance and nutrition of the plants. The quality of fruits and grapes is significantly diminished, with radiation impacting the chemical composition, including the content of sugars, organic acids, and phenolic compounds. In some cases, the antioxidant potential and organoleptic qualities of the products can be altered [13].

The increase in UV-B radiation due to ozone layer depletion has potentially harmful effects on plant growth and performance. Teramura [14] and Kramer et al. [15], studying the influence of UV-B radiation on the anatomical and morphological characteristics of plants, observed common induced changes such as reduced stature, decreased leaf area and total biomass, as well as alterations in biomass distribution among the different plant organs. Epidermal transmittance in the UV region decreases in irradiated leaves. This decrease is mainly associated with the stimulation of flavonoid biosynthesis and is considered a protective, screening response against the harmful effects of UV-B radiation. Mirecki and Teramura [16] indicate that both anatomical/morphological and physiological/biochemical factors contribute to plants' sensitivity to UV-B radiation. UV-B irradiated leaves also exhibited a decrease in stomata conductance compared to non-irradiated leaves. These reductions are significantly correlated with the observed decrease in photosynthesis rates. UV-B radiation also significantly reduced transpiration rates. Longo-Minnolo et al. [17] determined vegetation indices using the QGIS program by combining spectral bands detected with the raster method, as evaluating the water status of a crop is fundamental in implementing precision irrigation criteria in the field. Their results indicated that there is a weak correlation between the spectral bands and the traditional stem water potential during the rapid growth stage of fruit including grapes. Thus, Shakya [18] implemented and used thermal imaging as a technique in agricultural crop water management due to its efficiency in estimating canopy surface temperature and predicting crop water levels by integrating an UAV. This technique was able to address several difficulties, including the estimation of water in the plants in farms or fields, while considering officially induced variability or naturally existing water levels, with the help of high-resolution thermal images.

An updated description of the applications supported by UAVs in orchard management is presented by Zhang et al. [19] focusing on the diversity of data-processing techniques, including monitoring efficiency and accuracy. At the same time, they identified the gaps, examined the opportunities for UAV-based orchard management, discussed the performance of emerging technologies, and compared similar research providing technical and comprehensive support for the further exploitation of UAVs and a revolution in orchard management.

Understanding UV-B radiation intensity values thus becomes an important aspect in implementing protection strategies by developing and applying appropriate measures to shield crops from the harmful effects of radiation, minimizing the impact on the quality and quantity of agricultural products, and ensuring healthy plant growth.

Currently, research for environmental monitoring of orchards' fruit trees and grapevines focuses on developing and implementing advanced technologies to improve efficiency and precision in resource management and crop protection. The main issues that require solutions are the high labor costs, the difficulty of obtaining real-time data, and the lack of effective tools for early detection of plant stress caused by unfavorable environmental conditions such as drought, diseases, or pests.

The aim of this work included the development of an innovative modular digital system that can be easily integrated into a low-cost commercial drone for quantifying UV-B radiation values. This system, together with its other components, is designed to be a valuable tool for agronomists, domain experts, or farmers in surveillance and monitoring the health of crops in orchards and vineyards, ultimately ensuring that interventions are appropriate and effective. The main advantages of using UAVs (drones) in agriculture are real-time monitoring, accessibility in hard-to-reach areas, efficiency in data collection, and early problem detection. Strong environmental adaptability is another important advantage, as modern drones can operate in various weather conditions, such as moderate wind, fog, or temperature variations, on difficult terrain that is hard to access for traditional vehicles, or in wet or marshy areas. Therefore, the proposed aim led to the following research objectives:

(a) Designing adaptive hardware and software architectures for UV-B radiation monitoring systems;
(b) Ensuring compliance with local regulations regarding the use of drones and specialized sensors, as well as decision-support procedures and rules under conditions of uncertainty;
(c) Storing data in an easily accessible and analyzable format, preferably with location and time metadata for seamless integration into GIS systems.

This research aimed to create a prototype (with sensors and minicomputer) of an unmanned aerial system equipped with intelligent hardware and software technologies necessary for the supervision and monitoring of the health and growth of crops in orchards with vines and fruit trees, respectively monitoring the UV radiation and the battery current of the device. This modular system differs from the currently available ones in the simplicity of its realization/implementation; with low costs, it can be easily adapted to the environmental conditions specific to orchards and vineyards, and it offers an efficient and viable alternative to ordinary farmers. Additionally, the novelty of our study lies in the fact that such a modular system can be customized according to the specific needs of each agricultural operation, adapting to the conditions of orchards and vineyards. The integration of such a system with low-cost commercial drones makes the technology accessible and efficient for farmers, providing a viable alternative to the particularly expensive systems already on the market, such as the DJI Enterprise Ecosystem, which is inaccessible to regular farmers. Additionally, the simplicity of the solution adopted for the environmental monitoring system is the major difference compared to existing systems.

2. Materials and Methods

2.1. Route Planning

The use of unmanned aerial vehicles (UAVs –Manufacturer DJI, Shenzhen, Guangdong, China) in precision and smart agriculture, particularly for vine and fruit tree growth management, pest control, and irrigation efficiency, as well as for yield forecasting and selective harvesting, is described in [20]. It also discusses the importance of flight planning for drones because these have the potential to improve decision-making in orchard and vineyard management, although constraints such as limited flight time and weather conditions need to be considered.

Monitoring environmental conditions that affect crop growth and development by accurately measuring parameters with digital sensors for humidity, temperature, and UV radiation, as well as capturing aerial images and videos for visual analysis of plant health, or integrating with geographical information systems, GIS software, (WebDOME Lightning version), enables early detection of issues and the taking of proactive measures to optimize plant health and crop yield [21]. For this, it was first necessary to plan the drone route used in the present research.

Route planning for a drone (Figure 1) using Bézier curves involves utilizing these to define a smooth and controlled path between various points of interest (Figure 2).

Figure 1. Equipping the DJI Mini 4 Pro drone (Dà-Jiāng Innovations, Shenzhen, Guangdong, China) with the Vishay VEML 6075 digital sensor.

Figure 2. Route planning through waypoints (screenshot): the green circles represent intermediate points, numbered from 1 to 7, while the pink diamond located at the center of the flight path represents the point of interest (POI), noted with 1.

Bézier curves are often used in autonomous navigation to plan precise and controlled routes. To guide a drone from an initial position to a final position while following specific reference points that are randomly distributed within the workspace with predefined coordinates, predictive control and Bézier curve generation algorithms are applied. Generally, the quadratic Bézier curve algorithm is used to enable a mobile robot to avoid obstructing obstacles during flight maneuvers.

A quadratic Bézier curve is a parametric curve used in computer graphics and several related fields. In the literature, the Bézier curve algorithm has been used to generate trajectories for various systems. The equation for a Bézier curve of degree n is described by the following equation [22]:

$$P_{[t_0, t_1]}(h) = \sum_{i=0}^{n} B_i^n(h) \cdot P_i, \tag{1}$$

where P_i—are the i points on the curve and $B_i^n(h)$—is the Bernstein polynomial, t_0—is the initial time, t_i—is time correspondent to points i, h—is prediction horizon time, with values in the range $(0, \ldots, 1)$. This term $B_i^n(h))$ is determined by relation:

$$B_i^n(h) = \binom{n}{i} \left(\frac{h_1 - h}{h_1 - h_0}\right)^{n-i} \left(\frac{h - h_0}{h_1 - h_0}\right)^i \tag{2}$$

with $i \in \{0, 1, 2, \ldots, n\}$.

It is well known that if constructed with a large number of control points, Bézier curves become numerically unstable (Figure 3). For this reason, in practice, it is preferable to combine low-degree Bézier curves smoothly for route planning [23]. The basic requirement for route planning is to pass through the starting point and the final point at different desired speeds. The lowest degree of Bézier curve that can satisfy this requirement is three.
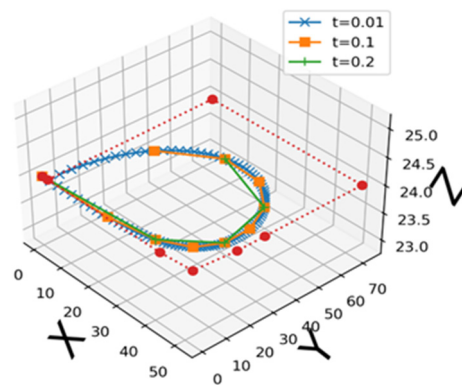
Figure 3. Tracking simulation results (blue, orange, green) over the planned paths (red).

Cubic Bézier curves used for route planning are denoted by:

$$P_{[t_{i-1},\, t_i]}(h) = \sum_{k=0}^{3} B_k^3(h) \cdot P_{k,i} \tag{3}$$

with $i \in \{0, \ldots, M\}$ where M is the total number of Bézier curves.

The planned trajectory $P(t)$ for, $t \in [t_0, t_M]$ is represented as:

$$P(h) = \left\{ P_{[t_{i-1}, t_i]}(h) \right\}, \; i \in \{0, \ldots, M\} \tag{4}$$

Route planning for a drone using Bézier curves involves several stages [24,25], including placing Bézier curves to connect flight segments and positioning control points, to ensure a smooth and safe trajectory, especially around turns.

The example in Figure 3 represents a numerical simulation performed in Python, version 3.12 for drone route planning using the Bezier algorithm. It is important to note that this algorithm was implemented because it is a pre-existing function in the software of the commercial drone used. The purpose of the simulation was to illustrate how the route planning function can be applied in the specific context of agricultural monitoring, without developing a new algorithm.

2.2. Hardware Components

2.2.1. The VEML6075 Sensor

The VEML6075 sensor, Vishay Intertechnology Inc., Malvern, PA, USA (Figure 4) is a UV radiation sensor that measures the intensity of UV-A and UV-B radiation. Two separate channels are used to detect UV-A (315–400 nm) and UV-B (280–315 nm) radiation (Figure 5a) [26]. Based on these measurements, an ultraviolet index (UVI) is calculated, providing an assessment of the potential for sunburn caused by UV radiation exposure [3]. An I2C interface (Figure 5b) ensures communication with a microcontroller or other host de-

vice. Compensation algorithms used in signal processing minimize interference effects and ensure more accurate measurements [27]. These algorithms eliminate any initial offset or sensor non-uniformity, ensuring that the recorded values accurately reflect the UV radiation present. Additionally, the sensor employs a filter to minimize the influence of visible light and infrared light, which could affect UV radiation measurements. The recorded values are adjusted to compensate for any contamination outside the UV spectrum. Since optical sensors can be sensitive to temperature changes, measurements are adjusted to account for temperature variations, ensuring accuracy in varying environmental conditions [28,29]. This aspect is particularly important. The sensor is used in various applications, including portable devices, weather stations, and environmental monitoring systems, to assess UV radiation exposure and help prevent sunburn and other related health issues.
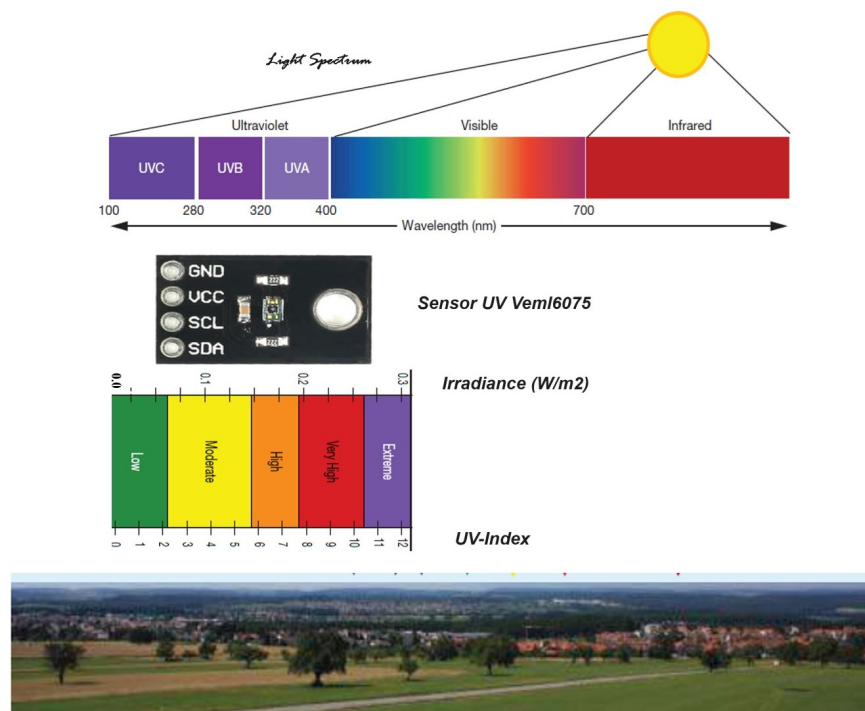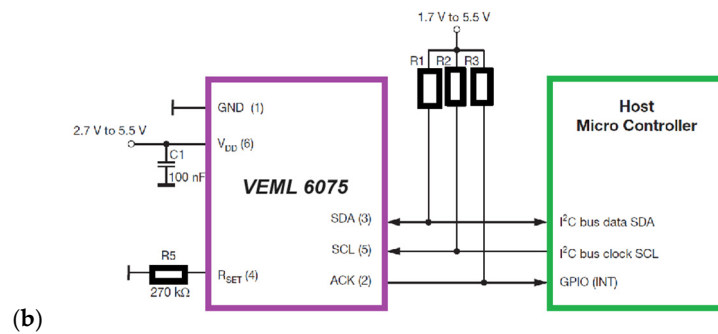

Figure 4. Measurement process, UV Index calculation, and alarm diagram with Vishay VEML6075 sensor.

(**a**)

Figure 5. *Cont.*

(b)
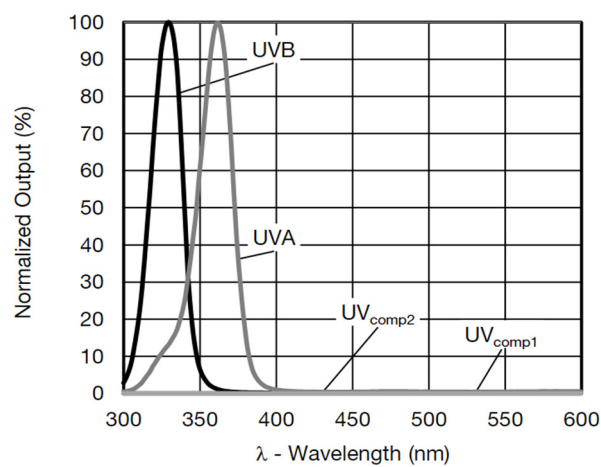
Figure 5. Sensor VEML6075 specifications: (**a**) spectral response function of sensors VEML6075; (**b**) I2C protocol interface.

2.2.2. UPS HAT Waveshare 19739

Functional characteristics of the UPS HAT Waveshare 19739 device (Waveshare Electronics, Shenzhen, Guangdong, China) are shown in Table 1.

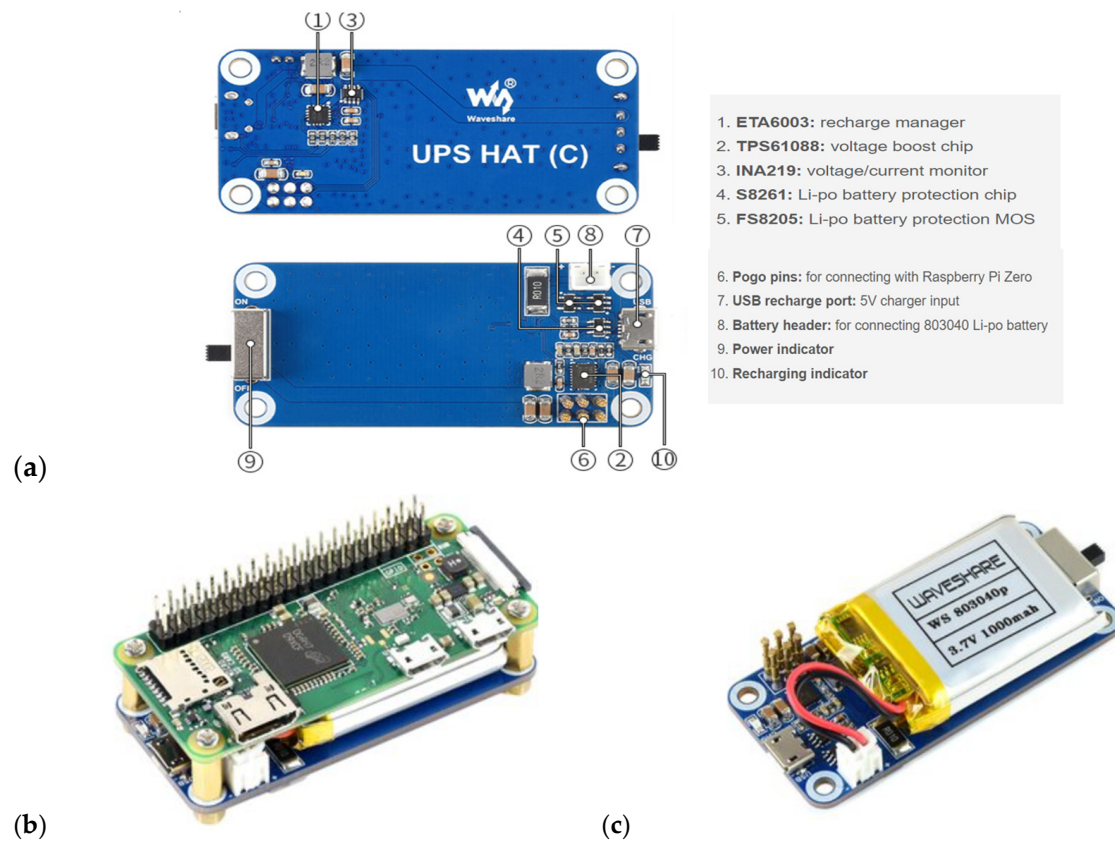**Table 1.** Functional characteristics of the UPS HAT Waveshare 19739 device.

Description	Specifications
Output voltage	5 V
Charger	5 V
Control bus	I2C
Battery	803040 Li-po 1000 mAh 3.7 V
Mounting hole size	3 mm
Dimensions	65 × 30 mm

The UPS HAT Waveshare 19739 (Figure 6a) is an accessory designed to provide an uninterrupted power supply for development boards, such as the Raspberry Pi Zero 2 W (Figure 6b). It mounts directly onto the development board via the GPIO interface and offers a range of functionalities and features that make it ideal for applications requiring continuity and reliability. The compact dimensions allow for easy integration without taking up much space or affecting access to other ports and connectors. It is equipped with a protection circuit to prevent damage to the battery (Figure 6c) and development board by avoiding situations of overcharging or complete discharge. The Waveshare 19739 HAT is equipped with a 1000 mAh Li-Po battery, Amperex Technology Limited, Hong Kong, China (see Figure 6c), which provides a significant energy reserve to keep the measurement device operational during the monitoring process [30]. The functional specifications of the device are detailed in Table 1. Additionally, it includes status LEDs that indicate the battery charging status and power level.

The connection with Raspberry Pi Zero series boards is made through the 6 Pogo pins mounted on the board [7]. For optimal battery charging while protecting the battery from overcharging and excessive discharge, an ETA6003 integrated circuit is used [31]. To increase the input voltage to a higher output voltage, the TPS61088 DC-DC boost regulator from Texas Instruments, Dallas, TX, USA can provide an output voltage of up to 5 V or more, depending on the circuit configuration. The TPS61088 is an essential component for applications requiring efficient voltage conversion, offering a reliable solution for voltage boosting in a variety of electronic devices [32].

Used in battery management systems (BMS) to measure the state of charge and energy consumption, the INA219 is a voltage and current monitoring integrated circuit manufactured by Texas Instruments [33,34]. It is designed to accurately measure the voltage over a range of up to ± 32 V between the power and reference terminals. It supports currents

up to ±3.2 A (depending on configuration and the values of the shunt resistors used). It uses the I2C interface for communication with microcontrollers and other devices, allowing measurements to be read and configured through a two-wire connection (SDA and SCL).

1. **ETA6003:** recharge manager
2. **TPS61088:** voltage boost chip
3. **INA219:** voltage/current monitor
4. **S8261:** Li-po battery protection chip
5. **FS8205:** Li-po battery protection MOS

6. **Pogo pins:** for connecting with Raspberry Pi Zero
7. **USB recharge port:** 5V charger input
8. **Battery header:** for connecting 803040 Li-po battery
9. **Power indicator**
10. **Recharging indicator**

Figure 6. The UPS HAT Waveshare 19739 diagram: (**a**) component elements of devices; (**b**) Raspberry Pi Zero 2 W attached on top; (**c**) 1000 mAh, 3.7 V Li-Po battery.

Protection chips, such as the S8261, are essential for the safe and efficient use of Li-Po batteries, which are sensitive to extreme operating conditions [35]. Additionally, in this category is the FS8205, a dual MOSFET chip that allows current switching both on the charging and discharging paths of the battery [36]. These chips are widely used in portable electronic devices, drones, electric vehicles, and other applications where battery reliability and safety are critical [37].

2.2.3. The Raspberry Pi Zero 2 W

The Raspberry Pi Zero 2 W (Raspberry Pi Foundation, Cambridge, UK) is a compact single-board computer developed by the Raspberry Pi Foundation, ideal for a wide range of applications that require a small and energy-efficient device [38]. Featuring a 1 GHz ARM Cortex-A53 quad-core processor, part of the Broadcom BCM2710A1 (Broadcom Inc., San Jose, CA, USA), system on chip (SoC), and 512 MB LPDDR2 SDRAM (Munich, Germany), it offers notable performance for various automation projects and internet of things (IoT) applications as a data collection node or control unit in IoT networks, or for controlling robots and other mobile devices [39]. The general-purpose input/output (GPIO) pins are compatible with other modules and accessories developed for Raspberry Pi, allowing users to add additional functionalities. It includes Wi-Fi (802.11b/g/n/ac (dual-band) for wireless connectivity) and Bluetooth (Bluetooth 4.2, Bluetooth Low Energy (BLE), Kirkland, WA, USA) for connecting peripheral devices. The operating system is compatible with Raspberry Pi OS (Raspbian) as well as other Linux distributions optimized for ARM [40–43].

2.2.4. The DJI Mini 4 Pro

The DJI Mini 4 Pro drone (Dà-Jiāng Innovations, Shenzhen, Guangdong, China) is one of the smallest and lightest drones in the DJI series, weighing less than 250 g. It is equipped with a high-performance camera capable of capturing high-resolution images and 4 K video at 60 frames per second. The camera features a 1-inch sensor, which provides superior image quality even in low-light conditions. Video stabilization is ensured by a 3-axis Gimbal, which helps capture smooth and stable footage.

The flight time is up to 34 min, depending on flight conditions and usage. It includes advanced obstacle avoidance systems with sensors on the front, rear, and bottom for safe navigation, reducing the risk of accidents. GPS and GLONASS technology allow precise positioning and accurately set the drone's trajectory. Intelligent features allow the drone to automatically return to the takeoff point in case of weak signal, low battery, or at the user's command. It supports video transmission over a distance of up to 10 km, providing a stable and high-quality data stream.

2.2.5. The Modular Proposed Prototype

The proposed prototype is a modular system integrated on a commercial drone, the DJI Mini 4 Pro, equipped with sensors for monitoring UV radiation and other environmental parameters. It includes a VEML6075 sensor (Vishay Intertechnology Inc., Malvern, PA, USA) that measures UV-A and UV-B radiation, a Raspberry Pi Zero 2 W (Raspberry Pi Foundation, Cambridge, UK) mini-computer for data processing, and a UPS HAT Waveshare 19739 module (Karlsruhe, Germany) that ensures continuous power supply for the system. The sensors collect data on UV radiation, while the drone, equipped with a high-resolution camera and advanced navigation systems, allows for efficient monitoring of agricultural areas, thus optimizing resource management and crop health. This modular architecture enables precise monitoring of UV radiation and other environmental parameters (moisture, temperature, etc.), integrating high-performance sensors and uninterrupted power solutions, all mounted on a lightweight and efficient drone.

The UAV used in this case is of the multi-rotor type, which can fly at different altitudes and is driven by four rotors. It has the advantage of passing over a specific location, using the Global Positioning System (GPS) system-based navigation, flying horizontally and vertically and only requiring a small takeoff and landing space. It is also easy to control and has high maneuverability. To enable the comparison among studies with the same or similar objectives, a UAV-based orchard and vineyard management framework was proposed (see Figure 4). Various data sources were acquired for different management scenarios showing notable differences. The Vishay VEML6075 sensor (Vishay Intertechnology Inc., Malvern, PA, USA) was applied to facilitate the monitoring of ultraviolet solar radiation. Next, decision indicators were extracted or calculated from the collected datasets utilizing advanced methodologies. Each "orchard or vineyard management" sub-category contains important aspects of the management activities, such as thermal drift correction, which aims to improve the accuracy of assessment of water stress. In each application scenario, different studies share the same main focus.

2.2.6. Data Processing and Storage Within the Modular System

The Raspberry Pi Zero 2 W (Raspberry Pi Foundation, Cambridge, UK) plays an essential role in managing the data flow in the modular UAV system, ensuring both collection of data from UV radiation sensors and other environmental factors, as well as the processing and storage of this data for later analysis. Below is a detailed overview of the process.

The VEML6075 sensor (Vishay Intertechnology Inc., Malvern, PA, USA) measures UV-A and UV-B radiation from the environment. It sends raw data to the Raspberry Pi via the I2C (inter-integrated circuit) interface. The I2C interface enables fast and efficient communication between the sensor and the Raspberry Pi, collecting the necessary information in real time.

Raspberry Pi (Raspberry Pi Foundation, Cambridge, UK) runs a dedicated Python script for data acquisition. This script periodically queries the sensor and receives data in the form of UV radiation values, which are temporarily stored in internal memory for further processing.

After collecting the raw data, Raspberry Pi processes it to filter out noise and correct measurement errors, such as temperature variations that could affect sensor accuracy. Compensation algorithms are used to adjust the measured values, ensuring their accuracy. This process is essential in the context of real-time UV radiation monitoring, as environmental conditions can change rapidly.

Then, after processing, the data are stored locally on the Raspberry Pi using a file system compatible with long-term storage solutions, such as FAT32 or ext4 (Vancouver, BC, Canada), depending on the external storage medium (SD card or USB drive, Hollywood, FL, USA).

At the flight mission is completed, the data are transferred to a central server or a computer for further analysis. This process can be automated via wireless connectivity (Wi-Fi integrated into the Raspberry Pi), sending the data in real time to an external database or storing it locally for later downloading.

The processed and stored data can later be analyzed using GIS software to visualize environmental conditions in different locations and identify potential issues, such as excessive UV radiation exposure. GIS platforms can generate maps indicating the vegetation status based on the collected data.

2.2.7. The Open-Source Platform WebODM

WebODM (Drone Mapping Software) is an open-source platform used for geospatial data processing and analysis, providing an accessible and flexible environment for generating 3D models, orthophotos, and other cartographic products from data collected using drones. WebODM is based on the OpenDroneMap platform (photogrammetry toolkit to process aerial imagery (from a drone) into maps and 3D models and allows for the automatic processing of aerial images to produce geospatial products useful in various applications, including precision agriculture.

In this study, WebODM was used to process the images captured by the DJI Mini 4 Pro drone during monitoring flights over orchards and vineyards. The captured images were processed to generate digital surface models (DSM) and orthophotos, which were then analyzed to assess vegetation conditions and detect potential issues, such as water stress or excessive UV radiation exposure.

The advantages of using the WebODM platform lie in its ability to transform raw drone data into useful geospatial products, facilitating the monitoring and analysis of conditions in orchards and vineyards, and contributing to the optimization of crop health and management.

3. Results and Discussion

3.1. Photogrammetry

The experimental location is a 3765 m^2 plot of clay soil with a fine texture but poor drainage, situated at the Faculty of Biotechnical Systems Engineering within the campus of the National University of Science and Technology POLITEHNICA Bucharest (take-off/landing coordinates 44.440218° N and 26.045350° E), as shown in Figure 7a. The site's topography is relatively homogeneous and flat. The plot is oriented north–south, with an average slope of less than 0.23%. Monitoring activities were conducted in an orchard containing various species, such as apple trees, pear trees, plum trees, cherry trees, peach trees, apricot trees, and sour cherry trees, located near the vineyard.

The experiments presented in this study, which can be classified as open-type operations, were carried out under maximum safety conditions concerning other aircraft, infrastructure, and individuals.

(**a**)

(**b**)
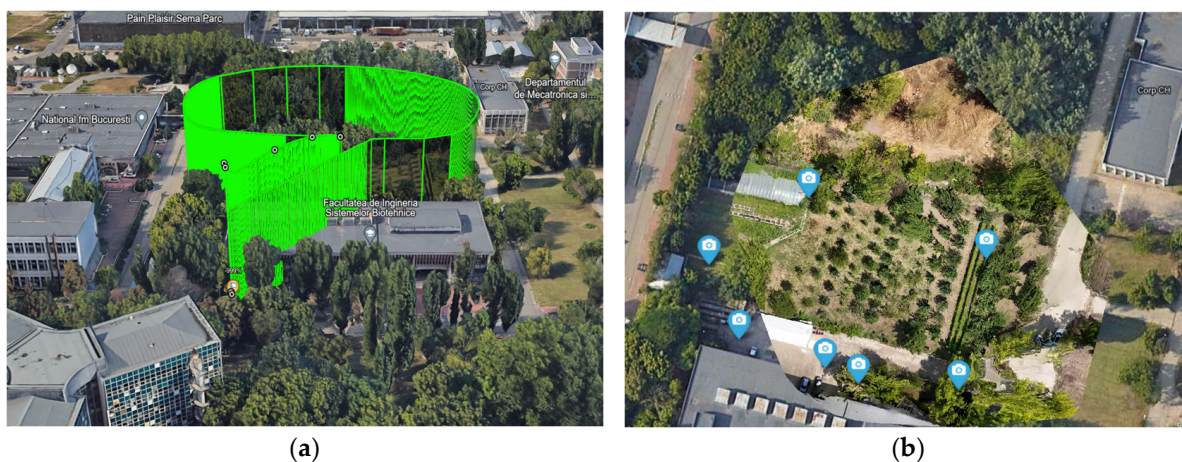
Figure 7. Location of the experiments at the National University of Science and Technology PO-LITEHNICA Bucharest Campus: (**a**) 3D visualization of the flight mission (Google Earth screenshot); (**b**) location of points along the route for image capture.

To analyze vegetation indices, several flight missions were conducted [44]. A photogrammetric test was performed to map the crop height by capturing images focused on the point of interest (POI) defined during the flight trajectory design (see Figure 2). Processing of aerial images captured at the selected points along the route (Figure 7b) and photogrammetry was carried out using the open-source platform WebODM.

Processing a digital surface model (DSM) involves several steps, from data acquisition to analysis [45]. Figure 8 illustrates the use of aerial photos taken by a drone equipped with a high-quality camera, capturing multiple overlapping images from different angles to create the 3D DSM. The camera featured a 1/1.3-inch CMOS sensor, with a photo resolution of 48 MP and a video resolution of up to 4 K at 60 fps. The lens used has an equivalent focal length of 24 mm, an aperture of f/1.7, and a field of view of 82.1°. The three-dimensional digital model (DSM) represents the elevation of features on the Earth's surface and includes all elements above ground level, such as buildings, trees, and other structures, to characterize and analyze the heights of these elements. The 2D element was removed by extending the 3D model to a certain height. Various parameters, such as the length, circumference, perimeter, and area of the building under reconstruction, were calculated using the DSM [46]. The WebODM platform uses structure from motion (SfM) technology to reconstruct 3D points based on photographs and then creates a point mesh from which the digital surface model is derived. This model can be used to analyze altitude variations and surface characteristics in a monitored region.


(**a**)

(**b**)
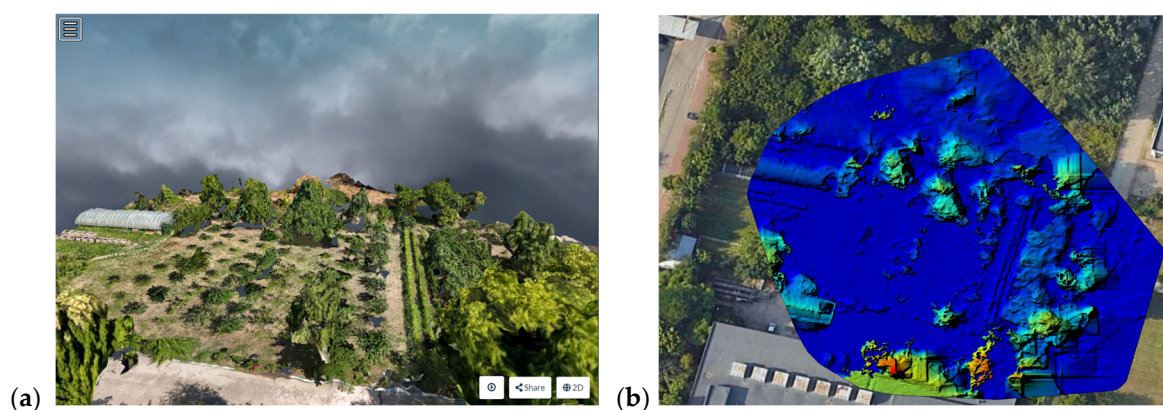
Figure 8. The control action digital surface model DSM: (**a**) orthophoto image; (**b**) DSM model.

The Green Leaf Index (GLI) is a vegetation index used to assess the presence and health of green vegetation. Like other vegetation indices, GLI is calculated based on the reflectance of light in different spectral bands and is used to highlight differences between green vegetation and other types of surfaces, as shown in Figure 9. The formula for calculating the GLI index is [47]:

$$GLI = (2G - R - B)/(2G + R + B) \tag{5}$$

where G is the reflectance value in the green band channel, R is the reflectance value in the red band channel, and B is the reflectance value in the blue band channel.
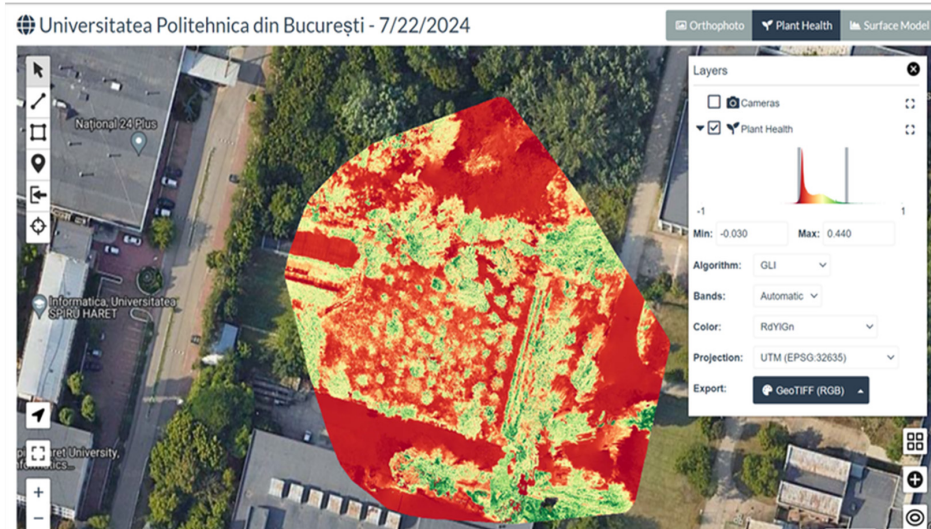

Figure 9. Green Leaf Index (GLI).

The GLI leverages the fact that green vegetation reflects more light in the green band and absorbs more light in the red and blue bands. By increasing the weight of the green channel and decreasing the contribution of the red and blue band channels, GLI enhances signals from green vegetation. Because it is simple to calculate and can be derived from images captured with standard RGB cameras, it is highly accessible for a wide range of applications in ecology, agriculture, and natural resource management [48,49].

To detect water content in vegetation and water-covered surfaces, a spectral index called the Normalized Difference Water Index (NDWI) was used. The NDWI helps identify areas with high moisture or water and is useful in various applications, including agricultural monitoring, water resource management, and natural disaster assessment [17]. The NDWI is calculated using reflectance values in specific spectral bands, typically the near-infrared (NIR) and green bands. The general formula/relationship for the NDWI is:

$$NDWI = (G + NIR)/(G - NIR). \tag{6}$$

Reflectance in the green band G (typically around 0.55 μm) was chosen because this wavelength is sensitive to leaf moisture and water content in vegetation. In our example, the WebODM platform generated a pseudo-NIR band based on algorithms that interpret data from other available spectral bands, providing an estimate of reflectance in the NIR spectrum and thus allowing the calculation of the NDWI. Reflectance in the near-infrared band (typically between 0.76 and 0.90 μm) is reduced in the presence of water, as water strongly absorbs this wavelength [50]. High positive NDWI values, as shown in Figure 10, indicate the presence of water or vegetation with high water content; healthy and moist vegetation has lower reflectance in the NIR band and higher reflectance in the green band, leading to positive NDWI values. Low-positive NDWI values suggest healthy vegetation but with lower water content or a moist area. Negative or near-zero values observed on the

NDWI index map in Figure 10 predominantly indicate dry soils, exposed soil surfaces, or vegetation stressed by water scarcity.
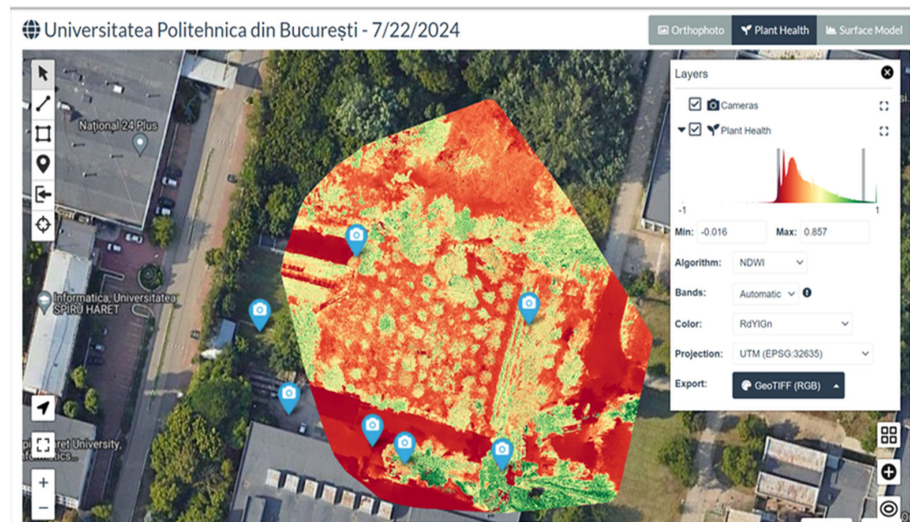

Figure 10. The NDWI or Normalized Difference Water Index.

To quantify vegetation density and reduce the influence of soil reflectance on measurements, the Soil Adjusted Vegetation Index (SAVI) was used. It is a modification of the Normalized Difference Vegetation Index (NDVI). The SAVI index (see Figure 11) is particularly useful in areas where vegetation is sparse or there is significant soil exposure, which can affect NDVI measurements. The calculation relationship for the SAVI index includes a soil adjustment factor, which helps to compensate for this effect [51], and is:

$$SAVI = (NIR - R) \times (1 + L) / (NIR + R + L) \tag{7}$$

where L is a soil adjustment factor that ranges between 0 and 1. A typical value for L is 0.5, but it can be adjusted depending on the specific soil and vegetation conditions.
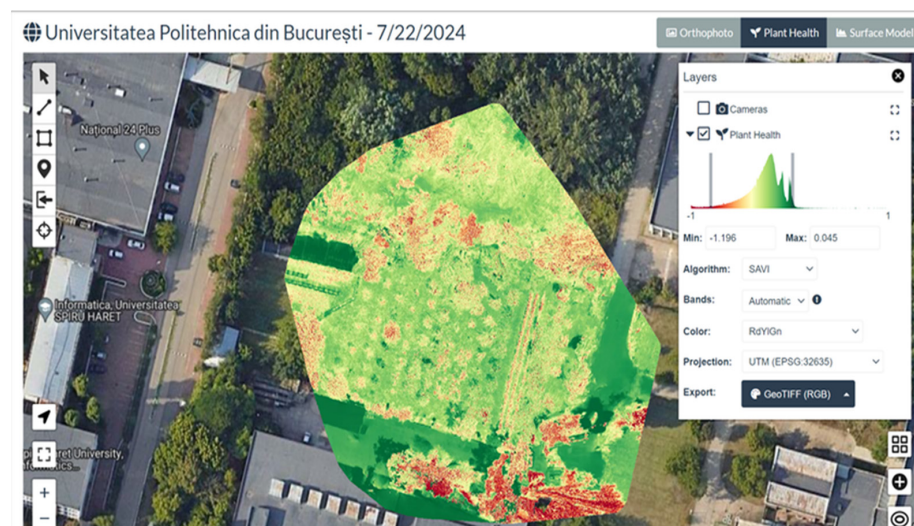

Figure 11. The SAVI or Soil Adjusted Vegetation Index.

The main advantage of the SAVI is that it enhances the ability to differentiate between vegetation and soil, particularly in conditions where vegetation is sparse and soil reflectance significantly influences measurements.

The Excess Green Index (EXG) is a vegetation index used in remote sensing to emphasize the presence of green vegetation in images. Unlike indices such as the NDVI or SAVI, which use information from the near-infrared spectrum, the EXG index relies solely on color channels from the visible spectrum, specifically differentiating between the green, red, and blue channels [52]. The formula/relationship for calculating the EXG index is:

$$EXG = 2G - R - B \tag{8}$$

High values of the EXG index, as shown in Figure 12, indicate a greater presence of green vegetation, while low or negative values indicate the absence of vegetation or the presence of other types of land cover, such as soil or buildings.
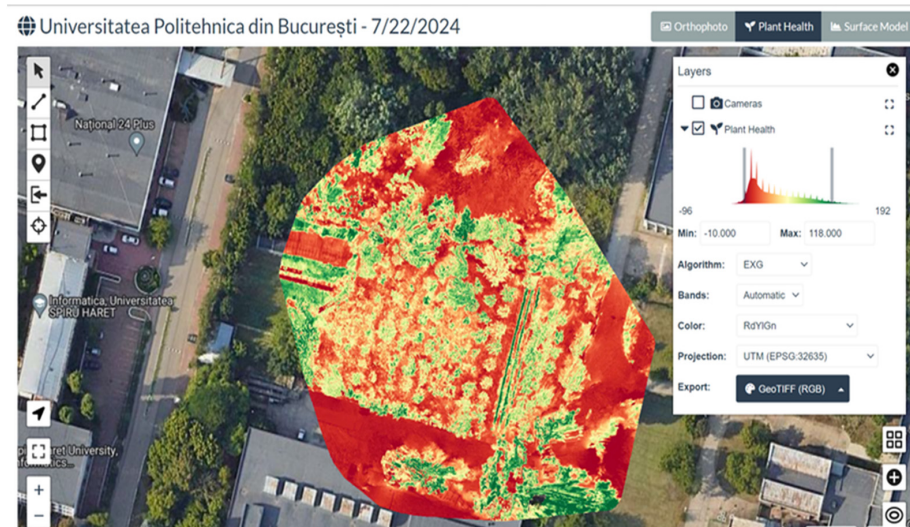
Figure 12. The EXG, or Excess Green Index.

The Burn Area Index (BAI) is a vegetation index used to identify and assess areas affected by wildfires. The BAI (Figure 13) is based on the differences in spectral reflectance between green vegetation and burned soil or vegetation [53,54].
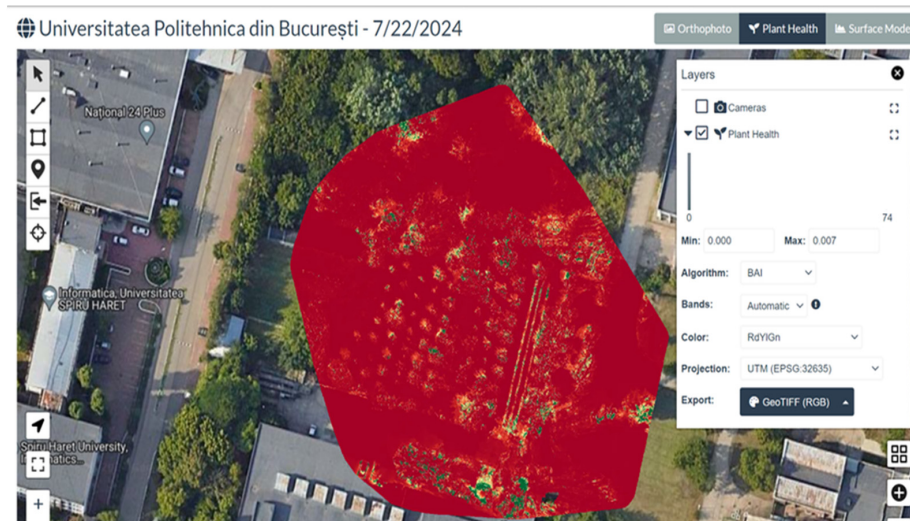
**Figure 13.** The BAI or Burn Area Index.

Green and healthy vegetation reflects more light in the visible and near-infrared spectra, while burned vegetation exhibits different spectral characteristics, often reflecting

less light in these ranges. The formula/relationship for calculating the BAI index (Burn Area Index) is:

$$BAI = \frac{1}{(0.1 - R)^2 + (0.06 - NIR)^2} \tag{9}$$

3.2. UV Radiation

Evaluating repeatability is essential to ensure that an instrument or measurement process produces reliable and consistent results. Measurement repeatability refers to the consistency and stability of results obtained when a measurement is repeated under the same conditions. To determine repeatability and deviations due to temperature, the UV sensor Veml6075 was exposed to constant irradiation for 1 min from a known 10 W source, with temperature variation measured using the Bosch BME 680 digital sensor [55], as shown in Figure 14.
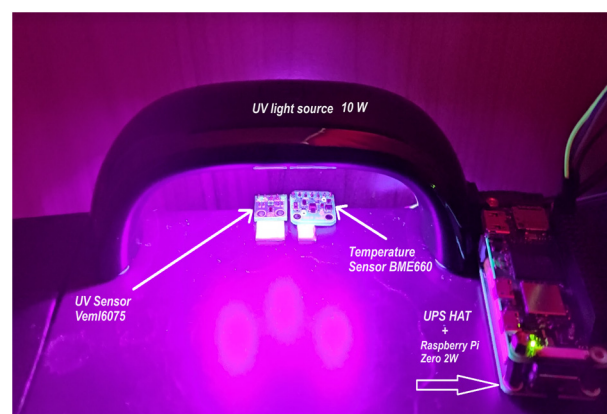
Figure 14. Stand testing the repeatbility data sensor VEML6075.

Four sets of consecutive measurements were taken, with repeatability assessed by calculating the coefficient of variation (CV), expressed as a percentage. This provides a relative measure of variation concerning the mean and is determined using the following formula/relationship:

$$CV = 100 \cdot \sigma / Mean \tag{10}$$

where σ—is the standard deviation and *Mean* is the mean of the series of values.

The coefficient of variation of 0.49% (*Mean* = 105 μW/cm^2; σ = 0.52 μW/cm^2) indicates good repeatability of the measurements, as the relative variation from the mean is small.

In Figure 15, the four datasets used to identify the temperature deviation coefficient of the VEML6075 sensor are presented. This dataset indicates a systematic change in measurements after irradiation (of nearly 2.5 °C) but without a significant increase in the variability of the measurements. The calculated temperature deviation coefficient of 1.093 (μW/cm^2)/°C indicates that the sensor remained consistent in its measurements [56], even though there was a systematic change in the measured values.

In Figure 16, the graph shows the variation of UV-B radiation over time measured with the VEML6075 sensor during the planned flight mission. The dataset does not indicate a significant increase in values within the range of 138–143 μW/cm^2 (with an average value of 140.74 μW/cm^2 and a standard deviation of 1.12). The coefficient of variation of 1.27% indicates that the sensor was stable in measurements. Figure 17 shows the histogram of the distribution of the obtained measurements, highlighting the variation and frequency of values recorded during the experiment. The histogram shows the frequency distribution for each bin. The x-axis represents the bins, and the y-axis shows the frequency of occurrences for each bin. The most frequent values were found in the range of 140 and 141, indicating a higher concentration of data values, around 61%, in these ranges.
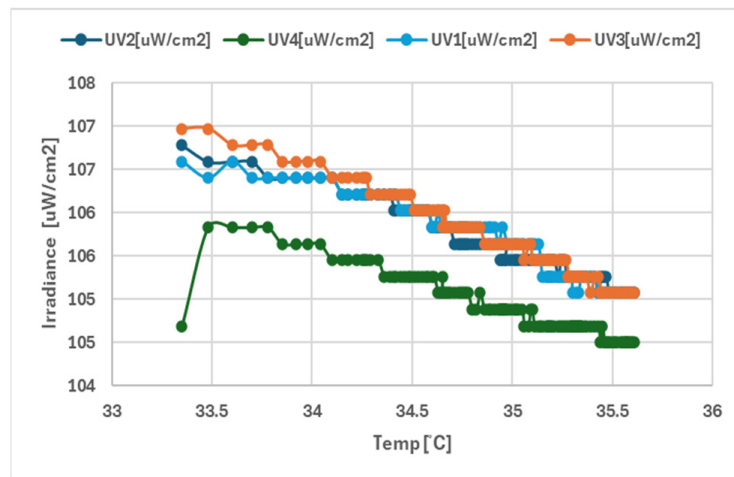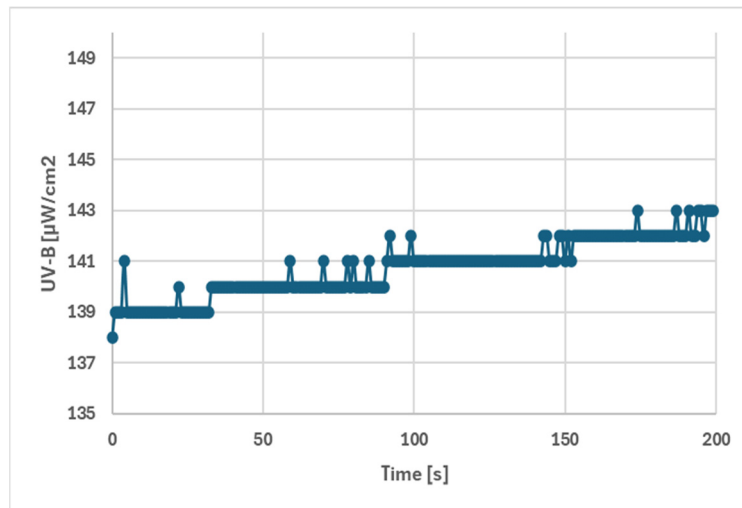
Figure 15. Drift temperature sensor VEML6075.

Figure 16. Evolution of UV-B radiation in function of flight time.
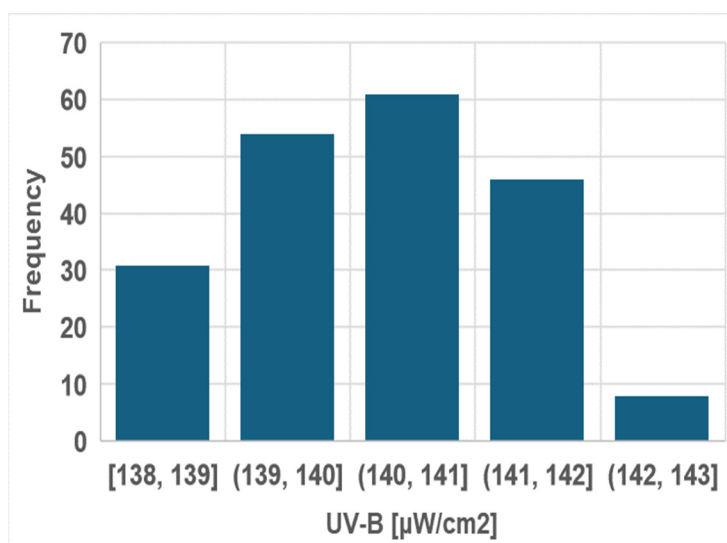

**Figure 17.** Testing the distribution data obtained with the VEML6075.

Very promising results were obtained by Heath (2023) [57] with a UV-sensitive camera and state-of-the-art object detection algorithms. The development of the proposed system,

being low-cost and highly scalable, proves that the UV spectrum can provide valuable information about crop flowers and opens up new opportunities for future research.

3.3. Flight Performance Analysis

Figure 18 presents the data obtained to monitor the battery of the energy-independent modular system used to measure UV radiation attached to the drone. To determine the absolute error (E_a), the difference between the measured value (V_m) and the reference value (V_r) was calculated, with the relationship:

$$E_a = \mid V_m - V_r \mid \tag{11}$$
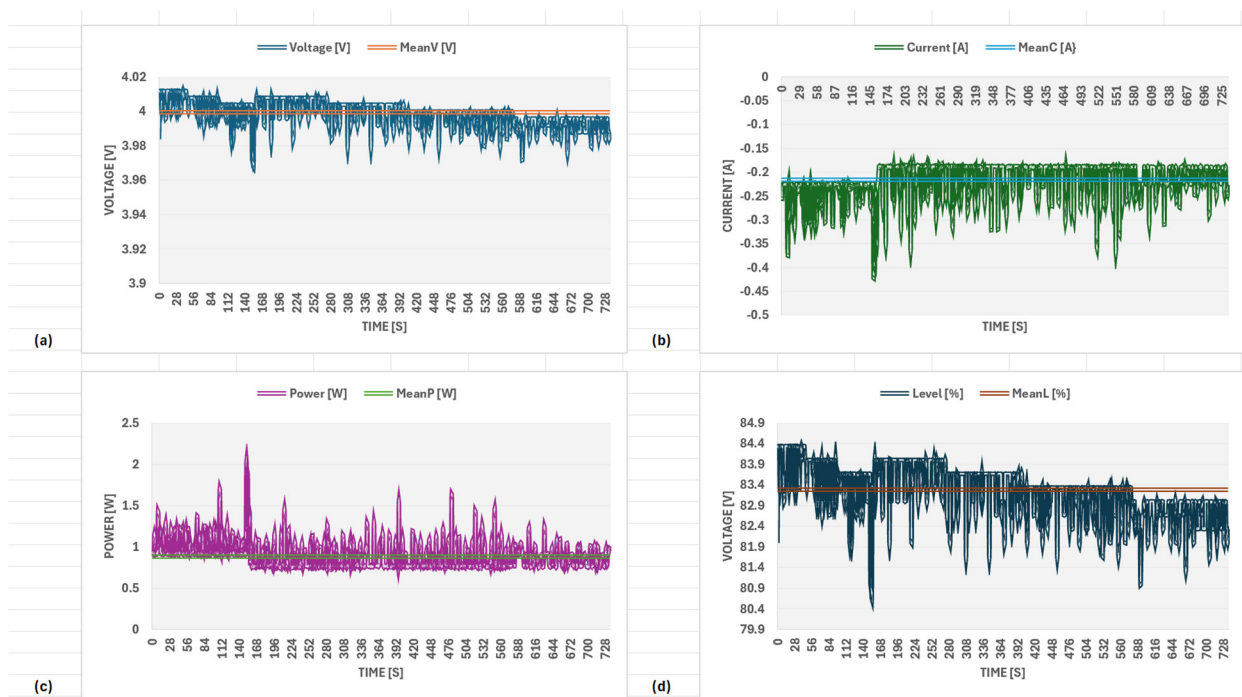
Figure 18. The energy consumption of the modular UV-B measurement system during monitoring operations: (**a**) voltage over time, showing the fluctuations around the mean voltage (MeanV) in volts (V); (**b**) current measurements over time, with the average current (MeanC) displayed to observe variations in amperes (A); (**c**) power consumption plotted over time, indicating instantaneous power against the mean power (MeanP) in watts (W); (**d**) battery level percentage over time, illustrating the battery discharge trend alongside the average level (MeanL) in percentage (%).

To determine the relative error (E_r), the ratio between the absolute error (E) and the reference value (V_r) was calculated, expressed as a percentage:

$$E_r = 100 * \frac{E_a}{V_r} \; (\%) \tag{12}$$

In Figure 18a, the graph of the voltage measured with the INA 219 sensor can be seen: it shows that the average voltage value was 3.99 ± 0.007 V, resulting in a relative error of 0.15%. The maximum error of the measured voltage was 0.78% in the standard configuration, while the minimum error was 0.02%. From Figure 18b, it can be observed that the average current consumed by the module was 0.215 ± 0.035 A, resulting in an average relative error of 12.81%. According to the technical specifications of the INA219 sensor, it can detect a bidirectional current of up to 3200 mA [58,59]. Figure 18c,d present the graphs of the calculated data for energy consumption and battery charge level. Figure 18c illustrates the power consumption measured in watts (W) of the system during monitoring

operations. The average consumption was 0.89 ± 0.16 W and varied depending on factors such as processor load, sensor activity, and other operational parameters [60,61]. Figure 18d shows the variation in battery charge level over time, from 84.4% to approximately 80.9%. The graph highlights how the battery discharged as the system operated, providing insight into battery life and energy consumption efficiency. The conclusion drawn from these results indicates that the INA219 sensor is accurate, and integrating these methods can monitor the energy consumption of autonomous mobile robots or industrial equipment.

Analyzing the aircraft's behavior during the flight mission was essential to ensure the success of future missions and optimize the aircraft's performance. This process helped identify and address issues, thereby improving the efficiency and safety of flight operations.

Communication between the drone and GPS satellites is fundamental for the navigation and efficient operation of UAVs. In Figure 19a, it can be seen that the drone's GPS module received signals from multiple satellites (the minimum number was 15, and the maximum was 24) to calculate the three-dimensional position (latitude, longitude, and altitude) with precision [62,63]. The use of a high-quality GPS antenna indicates excellent signal reception capability and minimal interference effects. The good GPS signal level, with a value of 5, as well as the number of connected satellites, shows that the drone had excellent GPS coverage and performed precise navigation.
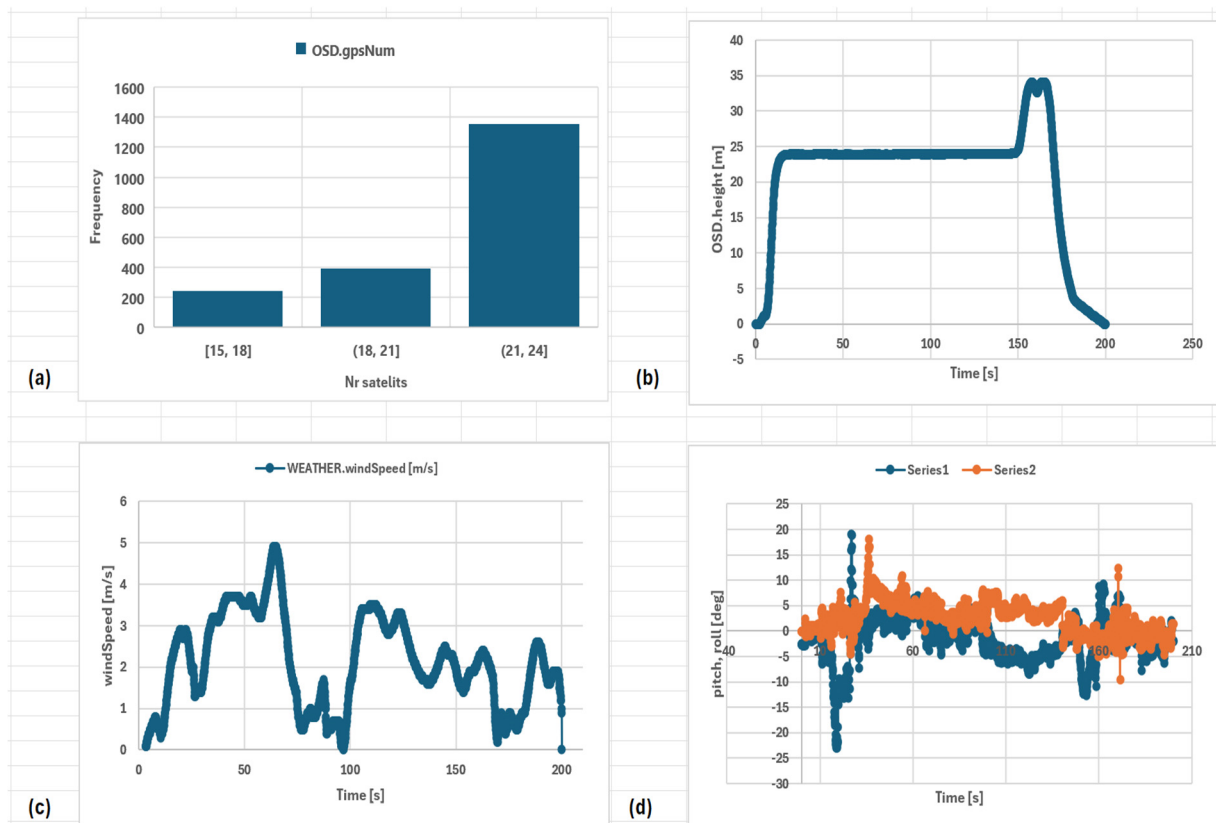

Figure 19. Analysis of the aircraft's behavior during the flight mission: (**a**) the number of GPS satellites connected during the mission; (**b**) the evolution of the aircraft's altitude; (**c**) the variation in wind speed; (**d**) the variation in pitch and roll angles.

The altitude measurement of a drone relative to the ground is performed using a barometric altimeter or a distance sensor and is used to avoid obstacles and maintain a constant flight level relative to the terrain. In the diagram in Figure 19b, the variation in the drone's altitude measured in meters is represented, with real-time information displayed on the remote-control screen. The figure shows that a constant flight level of 24 m was maintained along the planned trajectory. Then, to return to the takeoff position, the drone

ascended to an altitude of approximately 35 m to avoid certain obstacles, after which it landed at ground level, at the departure position.

The attitude of the drone represents the orientation of the drone's coordinate system relative to the inertial coordinate system (ground-based). It reflects the rotation of the drone around its x, y, and z axes. In this case, applying the right-hand rule resulted in the three classic movements encountered in aircraft: roll, pitch, and yaw. Wind speed has a strong impact on the drone's attitude and performance. Although artificial intelligence algorithms automatically adjust responses to commands based on wind conditions, improving stability and control, the drone's stabilization systems must work harder, leading to increased energy consumption and, consequently, shorter flight duration. Figure 19c shows the variation in wind speed recorded during the flight, while Figure 19d presents the flight controller's response, through the variation in pitch and roll angles, to counteract the effects of the wind and maintain the aircraft's stability [64].

Analysis of the aircraft's speed (especially during a flight mission) involves evaluating and interpreting data related to the aircraft's flight speed to understand its performance and optimize the flight [65,66]. Optimizing speed helps achieve clear and detailed images. Figure 20 presents speed data recorded during the planned mission, taking into account the impact of wind, temperature, and other weather conditions on the speed of movement. The horizontal speed values recorded in the flight file are shown in the graph in Figure 20a, while the ascent/descent speed values are displayed in Figure 20d. These graphs (in the middle section) show that during the planned route, the speed was relatively constant, and there were no issues with stability and maneuverability, highlighting the control capability to maintain a steady trajectory. The speed values recorded in the movements along the OX and OY axes of the coordinate system are presented in Figure 20b and 20c, respectively.
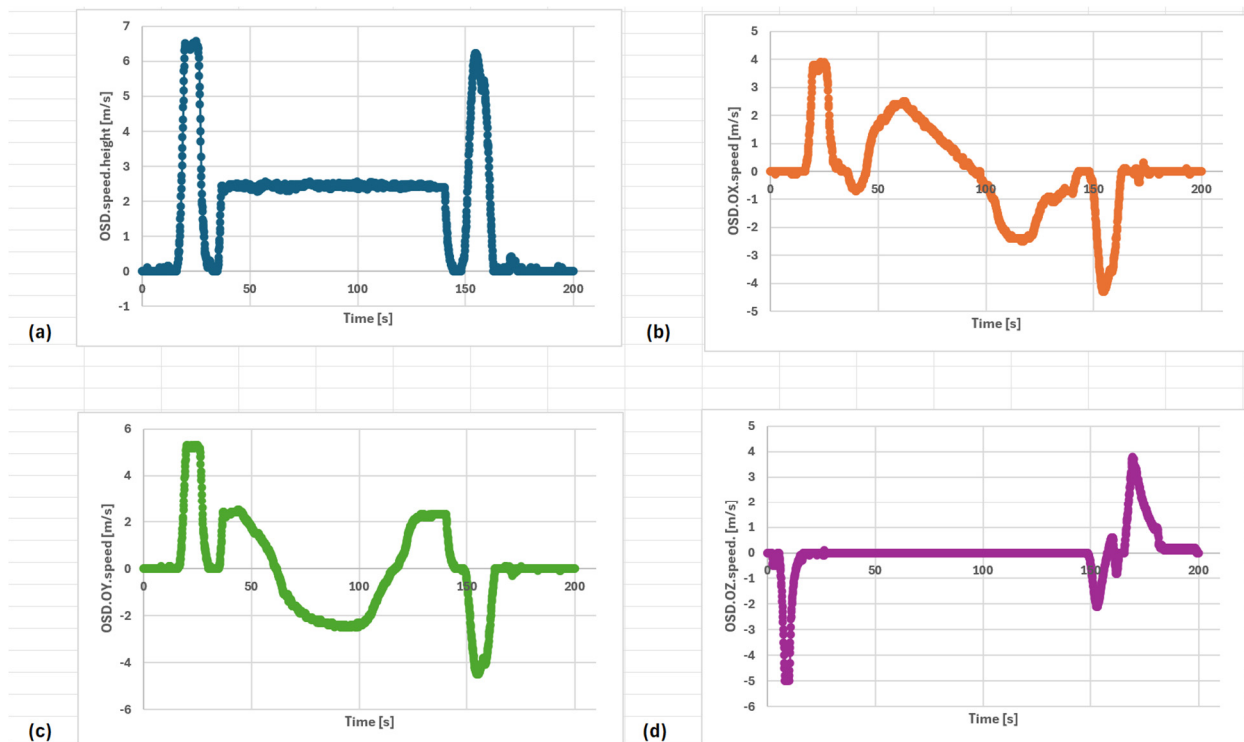
Figure 20. Analysis of the aircraft's speed during the flight mission: (**a**) horizontal speed; (**b**) speed in the OX direction; (**c**) speed in the OY direction; (**d**) speed in the OZ direction.

Generally, the speed values along the OX and OY axes are used to control and adjust the drone's trajectory, allowing precise navigation. The maximum speed achieved by the drone in the OX direction was 3.89 m/s, while in the OY direction, the maximum speed

was 5.29 m/s. Data recording occurred at an interval of 0.1 s. These data are also displayed on the remote-control screen, used for real-time monitoring of the aircraft's movement, ensuring precise navigation and effective mission management.

Therefore, based on the results obtained, the evaluation criteria of the modular system (prototype) used in this work can be established, namely:

- Data collection accuracy, determining the precision of UV radiation measurements and other environmental parameters compared to certified reference devices;
- Operational reliability, assessing the system's ability to repeatedly collect precise data, including during overloaded flight conditions and in various environmental conditions (temperature, humidity, etc.);
- Autonomy and energy consumption during flights, and the energy efficiency of system components, such as sensors and the Raspberry Pi module.
- Ease of implementation from the perspective of farmers, showing how quickly and easily the modules can be mounted and configured on a commercial drone.

On the other hand, the results obtained in this study are in line with previous research that has demonstrated the efficiency of using drones equipped with sensors for monitoring environmental parameters and crop health. For example, studies conducted by Hung et al. [1] and Aasen et al. [3] have shown the effectiveness of UAVs in quickly covering large areas and collecting high-resolution data. However, our study brings an additional contribution by integrating UV-B radiation monitoring, a parameter that has been less explored in previous research but can significantly impact plant health. Unlike the complex and expensive monitoring systems discussed by Popescu et al. [4], our modular solution offers a more accessible and easy-to-implement approach for farmers.

One of the major strengths of our system is its simplicity and flexibility, providing an accessible solution for farmers. The modular system can be customized according to the needs of each farm, and the use of low-cost commercial drones makes this technology much more affordable than the complex systems currently available on the market, such as the DJI Enterprise Ecosystem. However, there are a few limitations that should be noted. For example, adding additional equipment may exceed the weight limits for unlicensed drones, requiring special approvals for flight. Additionally, the system's autonomy can be affected under overload conditions or extreme temperatures, and sensor performance may vary depending on environmental factors. These limitations will be further investigated in future work, particularly regarding improving energy efficiency and reliability under extreme conditions.

4. Conclusions

UV-B radiation has a complex impact on orchards and vineyards, and understanding these effects through continuous surveillance and monitoring is essential in managing and optimizing agricultural production in the face of current climate changes. For this purpose, low-cost sensors were attached to the commercial drone used, to accurately measure the ultraviolet solar radiation.

The selection of a detection threshold for UV-B radiation of 2–5 W/m^2 for protecting vegetation depended on several factors that need to be considered. Among the principles used to establish the detection threshold are the type of crop or plant; the duration of exposure; local climatic conditions; the growth stages of the plants; existing data from the specialized literature; and the technical limits of the sensors.

The use of drones and GIS in analyzing plant health provides a significant advantage in precision agriculture management. This combination of technologies enables efficient monitoring, rapid interventions, and resource optimization, contributing to improved production and reduced costs. Flight path planning using Bézier curves allows for smooth and controlled trajectories, which are crucial for the safe and efficient operation of drones, especially in complex or urban environments.

Analysis of data obtained from sensors can provide valuable avenues for further development of mobile or modular equipment. In addition, the results of the analysis of

the state of the plantations with the model proposed in the GIS environment indicate the variations of the vegetation conditions and led to the identification of areas with problems such as water stress.

The study conducted fully demonstrated its utility by expanding the knowledge base in the field of surveillance and monitoring orchards and vineyards with a very low-cost solution compared to existing solutions.

Looking ahead, the use of AI algorithms will increasingly be required to automatically detect diseases, pests, or nutrient deficiencies based on drone images to predict future problems or optimize harvest of plantations.

Author Contributions: Conceptualization, G.I. and F.I.; methodology G.I. and F.I.; software, G.I. and C.T.; validation, G.I., C.T. and F.I.; formal analysis, C.T. and F.I.; investigation, G.I. and F.I.; resources, G.I., C.T. and F.I.; data curation, G.I., C.T. and F.I.; writing—original draft preparation, G.I.; writing—review and editing, G.I. and F.I.; visualization, G.I., C.T. and F.I.; supervision, G.I., C.T. and F.I.; project administration, F.I.; funding acquisition, G.I., C.T. and F.I. All authors have read and agreed to the published version of the manuscript.

Institutional Review Board Statement: Not applicable.

Informed Consent Statement: Not applicable.

Data Availability Statement: Data are contained within the article.

Conflicts of Interest: The authors declare no conflict of interest.

References

1. Hung, C.; Xu, Z.; Sukkarieh, S. Feature learning based approach for weed classification using high resolution aerial images from a digital camera mounted on a UAV. *Remote Sens.* **2014**, *6*, 12037–12054. [CrossRef]
2. Malveaux, C.; Hall, S.G.; Price, R. Using drones in agriculture: Unmanned aerial systems for agricultural remote sensing applications. In Proceedings of the American Society of Agricultural and Biological Engineers, Montreal, QC, Canada, 13–16 July 2014; p. 141911016. [CrossRef]
3. Aasen, H.; Honkavaara, E.; Lucieer, A.; Zarco-Tejada, P.J. Quantitative remote sensing at ultra-high resolution with UAV spectroscopy: A review of sensor technology, measurement procedures, and data correction workflows. *Remote Sens.* **2018**, *10*, 1091. [CrossRef]
4. Popescu, D.; Vlasceanu, E.; Dima, M.; Stoican, F.; Ichim, L. Hybrid sensor network for monitoring environmental parameters. In Proceedings of the 28th Mediterranean Conference on Control and Automation (MED), Saint-Raphaël, France, 15–18 September 2020; pp. 933–938. [CrossRef]
5. Stamate, M.A.; Pupaza, C.; Nicolescu, F.A.; Moldoveanu, C.E. Improvement of Hexacopter UAVs Attitude Parameters Employing Control and Decision Support Systems. *Sensors* **2023**, *23*, 1446. [CrossRef]
6. Digulescu, A.; Despina-Stoian, C.; Popescu, F.; Stanescu, D.; Nastasiu, D.; Sburlan, D. UWB Sensing for UAV and Human Comparative Movement Characterization. *Sensors* **2023**, *23*, 1956. [CrossRef] [PubMed]
7. Popescu, D.; Ichim, L.; Stoican, F. Orchard monitoring based on unmanned aerial vehicles and image processing by artificial neural networks: A systematic review. *Front. Plant Sci.* **2023**, *14*, 1237695. [CrossRef]
8. Signing, V.R.F.; Taamte, J.M.; Noube, M.K.; Abanda, Z.S.O.; Abba, H.Y. Real-time environmental radiation monitoring based on locally developed low-cost device and unmanned aerial vehicle. *J. Instrum.* **2023**, *18*, P05031. [CrossRef]
9. Ji, Y.Y.; Min, B.I.; Suh, K.S.; Joung, S.; Kim, K.P.; Park, J.H. Technical Status of Environmental Radiation Monitoring using a UAV and Its Field Application to the Aerial Survey. *J. Korea Soc. Ind. Inf. Syst.* **2020**, *25*, 31–39. [CrossRef]
10. Kezoudi, M.; Keleshis, C.; Antoniou, P.; Biskos, G.; Bronz, M.; Constantinides, C.; Sciare, J. The Unmanned Systems Research Laboratory (USRL): A new facility for UAV-based atmospheric observations. *Atmosphere* **2021**, *12*, 1042. [CrossRef]
11. Dou, H.; Niu, G.; Gu, M. Pre-harvest UV-B radiation and photosynthetic photon flux density interactively affect plant photosynthesis, growth, and secondary metabolites accumulation in basil (*Ocimum basilicum*) plants. *Agronomy* **2019**, *9*, 434. [CrossRef]
12. Cambrolle, J.; García, J.L.; Ocete, R.; Figueroa, M.E.; Cantos, M. Growth and photosynthetic responses to copper in wild grapevine. *Chemosphere* **2013**, *93*, 294–301. [CrossRef]
13. Bonilla, V.; Campoverde, B.; Yoo, S.G. A Systematic Literature Review of LoRaWAN: Sensors and Applications. *Sensors* **2023**, *23*, 8440. [CrossRef] [PubMed]
14. Teramura, A.H. Effects of ultraviolet-B radiation on the growth and yield of crop plants. *Physiol. Plant.* **1983**, *58*, 415–427. [CrossRef]

15. Kramer, G.F.; Krizek, D.T.; Mirecki, R.M. Influence of photosynthetically active radiation and spectral quality on UV-B-induced polyamine accumulation in soybean. *Phytochemistry* **1992**, *31*, 1119–1125. [CrossRef]

16. Mirecki, R.M.; Teramura, A.H. Effects of ultraviolet-B irradiance on soybean: V. The dependence of plant sensitivity on the photosynthetic photon flux density during and after leaf expansion. *Plant Physiol.* **1984**, *74*, 475–480. [CrossRef]

17. Longo-Minnolo, G.; Consoli, S.; Vanella, D.; Guarrera, S.; Manetto, G.; Cerruto, E. Appraising the stem water potential of citrus orchards from UAV-based multispectral imagery. In Proceedings of the IEEE International Workshop on Metrology for Agriculture and Forestry (MetroAgriFor), Pisa, Italy, 6–8 November 2023; pp. 120–125. [CrossRef]

18. Shakya, S. Unmanned Aerial Vehicle with Thermal Imaging for Automating Water Status in Vineyard. *J. Electr. Eng. Autom.* **2021**, *3*, 79–91. [CrossRef]

19. Zhang, C.; Valente, J.; Kooistra, L.; Guo, L.; Wang, W. Orchard management with small unmanned aerial vehicles: A survey of sensing and analysis approaches. *Precis. Agric.* **2021**, *22*, 2007–2052. [CrossRef]

20. Kasimati, A.; Lomis, A.; Psiroukis, V.; Darra, N.; Koutsiaras, M.G.; Papadopoulos, G.; Fountas, S. Chapter 5: Unmanned aerial systems applications in orchards and vineyards. In *Unmanned Aerial Systems in Agriculture*; Academic Press: New York, NY, USA, 2022. [CrossRef]

21. Ipate, G.; Voicu, G.; Dinu, I. Research on the use of drones in precision agriculture. *Univ. Politeh. Buchar. Bull. Ser.* **2015**, *77*, 1–12.

22. Al-Mayyahi, A.; Aldair, A.A.; Rashid, A.T. Intelligent Control of Mobile Robot Via Waypoints Using Nonlinear Model Predictive Controller and Quadratic Bezier Curves Algorithm. *J. Electr. Eng. Technol.* **2020**, *15*, 1857–1870. [CrossRef]

23. Choi, J.; Elkaim, G.H. Bezier Curve for Trajectory Guidance. In Proceedings of the World Congress on Engineering and Computer Science 2008, WCECS 2008, San Francisco, CA, USA, 22–24 October 2008.

24. Elhoseny, M.; Tharwat, A.; Hassanien, A.E. Bezier Curve Based Path Planning in a Dynamic Field using Modified Genetic Algorithm. *J. Comput. Sci.* **2018**, *25*, 339–350. [CrossRef]

25. Lai, R.; Wu, Z.; Liu, X.; Zeng, N. Fusion Algorithm of the Improved A* Algorithm and Segmented Bézier Curves for the Path Planning of Mobile Robots. *Sustainability* **2023**, *15*, 2483. [CrossRef]

26. Jiang, J. High Altitude Balloon. Ph.D. Thesis, Worcester Polytechnic Institute, Worcester, MA, USA, 2020.

27. Hassani, S.; Dackermann, U. A Systematic Review of Advanced Sensor Technologies for Non-Destructive Testing and Structural Health Monitoring. *Sensors* **2023**, *23*, 2204. [CrossRef] [PubMed]

28. Van de Giesen, N.; Steele-Dunne, S.C.; Jansen, J.; Hoes, O.; Hausner, M.B.; Tyler, S.; Selker, J. Double-Ended Calibration of Fiber-Optic Raman Spectra Distributed Temperature Sensing Data. *Sensors* **2012**, *12*, 5471–5485. [CrossRef]

29. Zhang, D.; Zhou, G. Estimation of Soil Moisture from Optical and Thermal Remote Sensing: A Review. *Sensors* **2016**, *16*, 1308. [CrossRef]

30. Cicioni, G.; De Angelis, A.; Janeiro, F.M.; Ramos, P.M.; Carbone, P. Battery Impedance Spectroscopy Embedded Measurement System. *Batteries* **2023**, *9*, 577. [CrossRef]

31. Zhang, Q.; Qu, M.; Liu, X.; Cui, Y.; Hu, H.; Li, Q.; Jin, M.; Xian, J.; Nie, Z.; Zhang, C. Three-in-One Portable Electronic Sensory System Based on Low-Impedance Laser-Induced Graphene On-Skin Electrode Sensors for Electrophysiological Signal Monitoring. *Adv. Mater. Interfaces* **2023**, *10*, 2201735. [CrossRef]

32. Xu, Q.; Yang, D.; Li, M.; Ren, X.; Yuan, X.; Tang, L.; Wang, X.; Liu, S.; Yang, M.; Liu, Y.; et al. Design and Verification of Piano Playing Assisted Hand Exoskeleton Robot. *Biomimetics* **2024**, *9*, 385. [CrossRef] [PubMed]

33. Lambert, J.; Monahan, R.; Casey, K. Power Consumption Profiling of a Lightweight Development Board: Sensing with the INA219 and Teensy 4.0 Microcontroller. *Electronics* **2021**, *10*, 775. [CrossRef]

34. Maroşan, A.; Constantin, G.; Gîrjob, C.E.; Chicea, A.L.; Crenganis, M. Real time data acquisition of low-cost current sensors acs712-05 and ina219 using raspberry pi, daqcplate and node-red. *Proc. Manuf. Syst.* **2023**, *18*, 51–59.

35. Huang, K.; Li, Z.; Yang, C. Design of Battery System of Emergency Power Supply for Auxiliary Fan in the Coal-Mine. In Proceedings of the International Conference on Control, Automation and Systems Engineering (CASE), Singapore, 30–31 July 2011; pp. 1–6. [CrossRef]

36. Guo, C.-Y.; Lin, T.-L.; Hsieh, T.-L. A Solar-Rechargeable Radiation Dosimeter Design for Radiation Hazard Zone Located with LoRa Network. *Quantum Beam Sci.* **2022**, *6*, 27. [CrossRef]

37. Stoica, D.; Gmal Osman, M.; Strejoiu, C.V.; Lazaroiu, G. Exploring Optimal Charging Strategies for Off-Grid Solar Photovoltaic Systems: A Comparative Study on Battery Storage Techniques. *Batteries* **2023**, *9*, 470. [CrossRef]

38. Yamanoor, N.S.; Yamanoor, S. High quality, low cost education with the Raspberry Pi. In Proceedings of the IEEE Global Humanitarian Technology Conference (GHTC), San Jose, CA, USA, 19–22 October 2017; pp. 1–5. [CrossRef]

39. Sunehra, D.; Jhansi, B.; Sneha, R. Smart Robotic Personal Assistant Vehicle Using Raspberry Pi and Zero UI Technology. In Proceedings of the 6th International Conference for Convergence in Technology (I2CT), Maharashtra, India, 2–4 April 2021; pp. 1–6. [CrossRef]

40. Schwart, M. *Building Smart Homes with Raspberry Pi Zero*; Packt Publishing Ltd.: Birmingham, UK, 2016.

41. Alarcón-Paredes, A.; Francisco-García, V.; Guzmán-Guzmán, I.P.; Cantillo-Negrete, J.; Cuevas-Valencia, R.E.; Alonso-Silverio, G.A. An IoT-based non-invasive glucose level monitoring system using raspberry pi. *Appl. Sci.* **2019**, *9*, 3046. [CrossRef]

42. Halfacree, G. *The Official Raspberry Pi Beginner's Guide: How to Use Your New Computer*, 5th ed.; Raspberry Pi Press: Cambridge, UK, 2023.

43. Janakiram, S.; Babu, M.; Jain, S.; Rai, R.; Mohan, R.; Safonova, M.; Murthy, J. Development Of Raspberry Pi-based Processing Unit for UV Photon-Counting Detectors. *arXiv* **2024**, arXiv:2401.01443v2. [CrossRef]

44. Sona, G.; Passoni, D.; Pinto, L.; Pagliari, D.; Masseroni, D.; Ortuani, B.; Facchi, A. UAV multispectral survey to map soil and crop for precision farming applications. *Int. Arch. Photogramm. Remote Sens. Spat. Inf. Sci.* **2016**, *41*, 1023–1029. [CrossRef]

45. Alganci, U.; Besol, B.; Sertel, E. Accuracy Assessment of Different Digital Surface Models. *ISPRS Int. J. Geo-Inf.* **2018**, *7*, 114. [CrossRef]

46. Kim, S.; Rhee, S.; Kim, T. Digital Surface Model Interpolation Based on 3D Mesh Models. *Remote Sens.* **2019**, *11*, 24. [CrossRef]

47. Lu, Z.; Deng, L.; Lu, H. An improved LAI estimation method incorporating with growth characteristics of field-grown wheat. *Remote Sens.* **2022**, *14*, 4013. [CrossRef]

48. Thanyapraneedkul, J.; Muramatsu, K.; Daigo, M.; Furumi, S.; Soyama, N.; Nasahara, K.N.; Muraoka, H.; Noda, H.M.; Nagai, S.; Maeda, T.; et al. A Vegetation Index to Estimate Terrestrial Gross Primary Production Capacity for the Global Change Observation Mission-Climate (GCOM-C)/Second-Generation Global Imager (SGLI) Satellite Sensor. *Remote Sens.* **2012**, *4*, 3689–3720. [CrossRef]

49. Ribeiro, A.L.A.; Macie, G.M.; Siquieroli, A.C.S.; Luz, J.M.Q.; Gallis, R.B.d.A.; Assis, P.H.d.S.; Catão, H.C.R.M.; Yada, R.Y. Vegetation Indices for Predicting the Growth and Harvest Rate of Lettuce. *Agriculture* **2023**, *13*, 1091. [CrossRef]

50. Ngo Thi, D.; Ha, N.T.T.; Tran Dang, Q.; Koike, K.; Mai Trong, N. Effective band ratio of landsat 8 images based on VNIR-SWIR reflectance spectra of topsoils for soil moisture mapping in a tropical region. *Remote Sens.* **2019**, *11*, 716. [CrossRef]

51. Zhen, Z.; Chen, S.; Yin, T.; Chavanon, E.; Lauret, N.; Guilleux, J.; Gastellu-Etchegorry, J.P. Using the negative soil adjustment factor of soil adjusted vegetation index (SAVI) to resist saturation effects and estimate leaf area index (LAI) in dense vegetation areas. *Sensors* **2021**, *21*, 2115. [CrossRef]

52. Zheng, H.; Cheng, T.; Li, D.; Zhou, X.; Yao, X.; Tian, Y.; Zhu, Y. Evaluation of RGB, color-infrared and multispectral images acquired from unmanned aerial systems for the estimation of nitrogen accumulation in rice. *Remote Sens.* **2018**, *10*, 824. [CrossRef]

53. Fornacca, D.; Re, G.; Xiao, W. Evaluating the best spectral indices for the detection of burn scars at several post-fire dates in a mountainous region of Northwest Yunnan, China. *Remote Sens.* **2018**, *10*, 1196. [CrossRef]

54. Han, A.; Qing, S.; Bao, Y.; Na, L.; Bao, Y.; Liu, X.; Wang, C. Short-term effects of fire severity on vegetation based on sentinel-2 satellite data. *Sustainability* **2021**, *13*, 432. [CrossRef]

55. Sunny, A.I.; Zhao, A.; Li, L.; Sakiliba, S.K. Low-cost IoT-based sensor system: A case study on harsh environmental monitoring. *Sensors* **2020**, *21*, 214. [CrossRef]

56. Goumopoulos, C. A high precision, wireless temperature measurement system for pervasive computing applications. *Sensors* **2018**, *18*, 3445. [CrossRef] [PubMed]

57. Heath, M. UV-Spectrum Remote UVA Imaging for Use in Precision Agriculture. Ph.D. Thesis, École de Technologie Supérieure, Montreal, QC, Canada, 2023.

58. Wiyadi, E.; Wati, A.; Hamzah, Y.; Umar, L. Simple IV acquisition module with high side current sensing principle for real time photovoltaic measurement. *J. Phys. Conf. Ser.* **2020**, *1528*, 012040. [CrossRef]

59. Prasetyawati, F.Y.; Harjunowibowo, D.; Fauzi, A.; Utomo, B.; Harmanto, D. Calibration and Validation of INA219 as Sensor Power Monitoring System using Linear Regression. *AIUB J. Sci. Eng. (AJSE)* **2023**, *22*, 240–249. [CrossRef]

60. Athanasadis, C.; Doukas, D.; Papadopoulos, T.; Chrysopoulos, A. A scalable real-time non-intrusive load monitoring system for the estimation of household appliance power consumption. *Energies* **2021**, *14*, 767. [CrossRef]

61. Khudhair, A.B.; Hussein, F.I.; Obeidi, M.A. Creating a LabVIEW Sub VI for the INA219 sensor for detecting extremely low-level electrical quantities. *Al-Khwarizmi Eng. J.* **2023**, *19*, 88–97. [CrossRef]

62. Upadhyay, J.; Rawat, A.; Deb, D. Multiple drone navigation and formation using selective target tracking-based computer vision. *Electronics* **2021**, *10*, 2125. [CrossRef]

63. Liu, S.; Lu, H.; Hwang, S.H. Three-Dimensional Indoor Positioning Scheme for Drone with Fingerprint-Based Deep-Learning Classifier. *Drones* **2024**, *8*, 15. [CrossRef]

64. Stamate, M.A.; Nicolescu, F.A.; Pupaza, C. Study regarding flight autonomy estimation for hexacopter drones in various equipment configurations. *Proc. Manuf. Syst.* **2020**, *15*, 81–90.

65. Chu, T.; Starek, M.J.; Berryhill, J.; Quiroga, C.; Pashaei, M. Simulation and characterization of wind impacts on UAS flight performance for crash scene reconstruction. *Drones* **2021**, *5*, 67. [CrossRef]

66. Doroftei, D.; De Cubber, G.; Bue, S.L.; De Smet, H. Quantitative Assessment of Drone Pilot Performance. *Drones* **2024**, *preprint*. [CrossRef]